

How large are curvature perturbations from slow first-order phase transitions? A gauge-invariant analysis

Xiao Wang ,  * Csaba Balázs ,  † Ran Ding ,  ‡ and Chi Tian ,  §

¹*School of Physics and Astronomy, Monash University, Melbourne 3800 Victoria, Australia*

²*School of Physics, Anhui University, 111 Jiulong Road, Hefei, Anhui, China 230601*

(Dated: January 22, 2026)

When strongly supercooled cosmological first-order phase transitions (FOPTs) are sufficiently slow, super-horizon inhomogeneities can be generated. We compute these super-horizon curvature perturbations by employing a gauge-invariant, multi-fluid formalism. By resolving the gauge ambiguities inherent in conventional separate-universe simulations, we demonstrate that Primordial Black Holes are unlikely to be produced by these super-horizon inhomogeneities. We also derive a fitting formula for the resulting curvature perturbations and discuss potential observational constraints on FOPTs imposed by limits on primordial curvature perturbations and associated scalar-induced gravitational waves.

I. INTRODUCTION

As one of the most appealing new physical phenomena in the early universe, cosmological first-order phase transitions (FOPTs) have been extensively studied. Such intriguing processes may occur when some fundamental symmetries are broken as the Universe cools down after inflation. These phase transitions may not only explain the observed cosmological baryon asymmetry [1–5], but may also serve as a predominant source of the stochastic gravitational-wave background (SGWB) [6–12], for which preliminary evidence in the nanohertz band has been reported by recent pulsar timing array (PTA) observations [13–17].

If the SGWB signal in recent PTA datasets was attributed to FOPTs in the early universe, strongly supercooled FOPTs are favored [18], suggesting a possible domination of vacuum energy prior to these FOPTs. As a consequence, a short period of thermal inflation may occur. In addition to favoring strong FOPTs, the PTA data also indicates that these transitions should be slow, characterized by a relatively small inverse duration parameter $\beta/H_n \sim 10$, where H_n represents the Hubble parameter during nucleation. As a result, the bubble nucleation timescale can be comparable to the Hubble time. Given the stochastic nature of the Poissonian nucleation process, this leads to distinct nucleation histories across causally disconnected regions. If vacuum energy is also dominant, these variations in nucleation history can introduce large fluctuations in the total energy density of these regions, ultimately generating super-horizon inhomogeneities [19, 20].

These large scale inhomogeneities not only induce curvature perturbations [19, 21] and are therefore subject to current or projected constraints [19, 22, 23], but, as

suggested in Ref. [21, 24–27], can also exceed the primordial black hole (PBH) formation threshold and lead to the production of PBHs. Furthermore, according to Ref. [24], when these inhomogeneous modes re-enter the horizon following thermal inflation, scalar-induced gravitational waves (SIGWs) can be generated. The amplitudes of these SIGWs are comparable to those of the conventional SGWB arising from bubble collisions or the radiation fluid, making them detectable by PTAs or other next-generation gravitational wave observatories.

These rich observational consequences are direct results of the super-horizon density contrasts induced by slow and strong FOPTs. However, as first pointed out by Ref. [20], caution must be taken when evaluating the gravitational effects arising from these density contrasts due to potential gauge ambiguities. Such density contrasts typically originate from statistical fluctuations in the bubble nucleation history and are computed by separate universe simulations without accounting for gravitational effects. When determining the gravitational perturbations induced by these inhomogeneities, gauge ambiguities arise because both the density contrast and the metric perturbations are gauge dependent.

In this study, we present a gauge-invariant framework to evaluate the gravitational consequences of large-scale inhomogeneities generated by a FOPT. Our methodology is based on the conventional formalism for multi-fluid systems, which enables the computation of gauge-invariant quantities, such as comoving curvature perturbations, without relying on a gauge-specific density contrast. Similarly as in [20], we find that the production of both PBHs and SIGWs is significantly suppressed compared to previous studies. Utilizing the derived fitting formula relating gauge-invariant comoving curvature perturbations to phase transition parameters, we analyze the observational implications arising from current and projected constraints on primordial curvature perturbations, as well as from potential SIGW signals in the PTA data.

* xiao.wang1@monash.edu

† csaba.balazs@monash.edu

‡ Corresponding author: dingran@mail.nankai.edu.cn

§ Corresponding author: ctian@ahu.edu.cn

II. THEORY OF COSMOLOGICAL FIRST-ORDER PHASE TRANSITIONS

In the standard framework for FOPTs, the nucleation rate of true vacuum bubbles is given by

$$\Gamma = H_n^4 \exp[\beta t], \quad (1)$$

where H_n is the Hubble parameter at the nucleation time t_n (which has been set to $t_n = 0$) and β describes the nucleation rate.

Once true-vacuum bubbles are generated, during the expansions of the bubbles, vacuum energy is transferred into the energy of the radiation, whose background average follows the continuity equation

$$\dot{\rho}_r + 4H\rho_r = -\dot{\rho}_V, \quad (2)$$

where ρ_r and ρ_V are the background energy density of the radiation and vacuum, respectively. The vacuum energy density ρ_V can be evaluated from the average false vacuum fraction $\bar{F}(t)$ [28, 29] by $\rho_V = \bar{F}(t)\Delta V$, where $\bar{F}(t)$ starts from 1 and ends at 0 after the FOPT, and ΔV denotes the vacuum energy density difference between the true and false vacua. The quantity $\bar{F}(t)$ can be estimated by

$$\bar{F}(t) = \exp\left[-\frac{4\pi}{3}\int_{-\infty}^t dt' \Gamma(t') a(t')^3 R(t, t')^3\right], \quad (3)$$

where $R(t', t)$ is the comoving radius of a bubble nucleated at time t' . During the thermal inflation driven by supercooled FOPTs, at the percolation time, the comoving Hubble radius will reach a minimum value, corresponding to a largest comoving wave number $k_{\max} = a(T_{\text{reh}})H(T_{\text{reh}})$, with T_{reh} being the reheating temperature. After percolation, modes with wave number $k < k_{\max}$ re-enter the horizon.

As suggested in Refs. [19, 24, 30], if a strongly supercooled FOPT occurred with a low nucleation rate (β is small), the Poisson nature of the bubble nucleation processes will induce significant variations in the nucleation history at super-Hubble scales. Since the energy density of the radiation fluid decreases as $a(t)^4$ while the vacuum energy remains constant, a delayed nucleation within a given Hubble patch generally leads to a larger-than-average total energy density, described by a positive density contrast $\delta \equiv \delta\rho/\rho$. This phenomenon can be quantified by simulating nucleation histories and solving for the distinct time-evolutions of the density fields across a large ensemble of independent super-Hubble patches, an approach analogous to the conventional “separate universe” picture [31]. Ref [24] provides a powerful toolkit `DeltaPT` to effectively facilitate such simulations.

However, these separate universe bubble nucleation simulations, such as in `DeltaPT`, are usually performed without specifying a gauge. We therefore denote the density contrast derived from such simulations as δ_{NG} (no gauge). As first highlighted in [20], ambiguities arise

when identifying this density contrast with its counterpart in gravitational perturbation theory, which in turn affects the subsequent estimates of the PBH abundance or the magnitude of curvature perturbations. In this work, rather than associating the results of `DeltaPT` or similar simulations with a particular gauge choice, we assume that the density contrasts δ_{NG} can be approximated, at linear order, by those computed on a specific but unknown time-slicing. This assumption enables the application of gauge-invariant formalisms. Utilizing the established formalism for multiple interacting fluids, detailed in the following section, we compute the curvature perturbations in a gauge-invariant manner.

III. LARGE-SCALE CURVATURE PERTURBATION FOR MULTIPLE INTERACTING FLUIDS

In this section, we outline the formalism for computing the curvature perturbation in the presence of multiple interacting fluids. For a comprehensive treatment, we refer the reader to Refs. [32, 33].

A. Background equations

Friedmann’s equations and the corresponding time evolution of the Hubble parameter are

$$H^2 = \frac{8\pi G}{3}\rho, \quad (4)$$

$$\dot{H} = -4\pi G(\rho + P). \quad (5)$$

If the universe consists of multiple component fluids which satisfy

$$\sum_{\alpha} \rho_{\alpha} = \rho, \quad \sum_{\alpha} P_{\alpha} = P, \quad (6)$$

the continuity equation for each component is given by

$$\dot{\rho}_{\alpha} = -3H(\rho_{\alpha} + P_{\alpha}) + Q_{\alpha}, \quad (7)$$

where Q_{α} represents the energy transfer rate to the α -fluid due to the interaction between different fluid components. Conservation of total energy implies that

$$\sum_{\alpha} Q_{\alpha} = 0. \quad (8)$$

As an example, for a universe consisting of two primary components, radiation and vacuum, the continuity equation for the radiation component (Eq. 2) is recovered by setting $\alpha = r$, $Q_r = -\dot{\bar{F}}(t)\Delta V$, and using the radiation equation of state, $P_r = \rho_r/3$.

B. Perturbed equations

In standard linear perturbation theory, the most general form of the line element for the spatially-flat FLRW

$$ds^2 = -(1 + 2\phi)dt^2 + 2a\partial_i B dt dx^i + a^2 [(1 - 2\psi)\delta_{ij} + 2\partial_i \partial_j E] dx^i dx^j, \quad (9)$$

where ψ and ϕ represent the gauge-dependent curvature perturbation and the lapse function, respectively.

With this perturbed metric, the gauge-invariant definition of the total curvature perturbations can be defined as

$$\zeta \equiv -\psi - H \frac{\delta \rho}{\dot{\rho}}, \quad (10)$$

which coincides with the curvature perturbation ψ for a uniform total-density slicing ($\delta \rho = 0$). We can also define another gauge-invariant curvature perturbation \mathcal{R} as

$$\mathcal{R} \equiv \psi - Ha(v + B), \quad (11)$$

where v is the scalar velocity potential. This is the so-called comoving curvature perturbation, coinciding with ψ on hypersurfaces orthogonal to worldlines comoving with the fluid. These two gauge-invariant equations have the relation

$$\frac{k^2}{a^2} \Psi = 3\dot{H}(\mathcal{R} + \zeta), \quad (12)$$

where another gauge-invariant curvature perturbation $\Psi \equiv \psi + H\sigma_s$ is introduced and $\sigma_s \equiv a^2 \dot{E} - aB$ is the scalar shear. Therefore, at super-Horizon scales ($k^2/(aH)^2 \ll 1$), $R \approx -\zeta$.

From the perturbed continuity equations at super-horizon scales (see refs. [31–33] for more details), the time evolution for the total density curvature perturbation is

$$\dot{\zeta} = -\frac{H}{\rho + P} \delta P_{\text{nad}}, \quad (13)$$

where the total non-adiabatic pressure perturbation δP_{nad} can be split into two parts,

$$\delta P_{\text{nad}} \equiv \delta P_{\text{intr}} + \delta P_{\text{rel}}. \quad (14)$$

The first part represents the intrinsic entropy perturbation from each fluid

$$\delta P_{\text{intr}} = \sum_{\alpha} \delta P_{\text{intr},\alpha}, \quad (15)$$

where intrinsic non-adiabatic pressure perturbation of each fluid is given by

$$\delta P_{\text{intr},\alpha} \equiv \delta P_{\alpha} - c_{\alpha}^2 \delta \rho_{\alpha}. \quad (16)$$

background and scalar metric perturbations is described by [34, 35]

Here, the adiabatic sound speed of α -fluid is defined as $c_{\alpha}^2 \equiv \partial P_{\alpha} / \partial \rho_{\alpha}$. By this definition, for any fluid with a definite equation of state of the form $P_{\alpha} = P_{\alpha}(\rho_{\alpha})$, the intrinsic non-adiabatic pressure perturbation, $\delta P_{\text{intr},\alpha}$, must vanish.

The second relative part of the non-adiabatic pressure perturbation can be computed by

$$\delta P_{\text{rel}} = -\frac{1}{6H\dot{\rho}} \sum_{\alpha,\beta} \dot{\rho}_{\alpha} \dot{\rho}_{\beta} (c_{\alpha}^2 - c_{\beta}^2) S_{\alpha\beta}, \quad (17)$$

where the relative entropy perturbation $S_{\alpha\beta}$ is defined as

$$S_{\alpha\beta} \equiv 3(\zeta_{\alpha} - \zeta_{\beta}) = -3H \left(\frac{\delta \rho_{\alpha}}{\dot{\rho}_{\alpha}} - \frac{\delta \rho_{\beta}}{\dot{\rho}_{\beta}} \right). \quad (18)$$

IV. LARGE-SCALE CURVATURE PERTURBATIONS FROM FOPTS

A. Methodology

At large scales, the dynamics of FOPTs can be effectively described by a system of multiple interacting fluids consisting of two primary components: radiation and vacuum. We therefore adopt this gauge-invariant formalisms and plug in both components to compute the comoving curvature perturbations from FOPTs. Firstly, we use `DeltaPT` to simulate a large-amount of bubble nucleation histories at various super-Hubble scales and nucleation rates β/H . For each super-horizon wave number $k > k_{\text{max}}$, we extract 50,000 different realizations of the nucleation history in a box of size $4\pi k^{-3}/3$, represented by 50,000 different functions of $F(t)$. Then, the same amount of different $\delta \rho_V(t) = (F(t) - \bar{F}(t))\Delta V$ are computed, where $F(t)$ is the false vacuum fraction computed for each causally disconnected patch. The corresponding $\rho_r(t)$ can then be obtained from the continuity equation Eq. (2).

Once the time evolution of $\delta \rho_V$ and $\delta \rho_r$ is determined, for each scale k and nucleation rate β/H , we integrate Eq. (13) up to t_k , the time at which the scale k re-enters the horizon. In calculating δP_{nad} , the intrinsic non-adiabatic perturbation δP_{intr} defined in Eq. (16) vanishes, as the sound speeds of both fluids are assumed to be constant ($c_r^2 = 1/3$ and $c_V^2 = -1$), suggesting a definite equation of state. For the remaining relative component

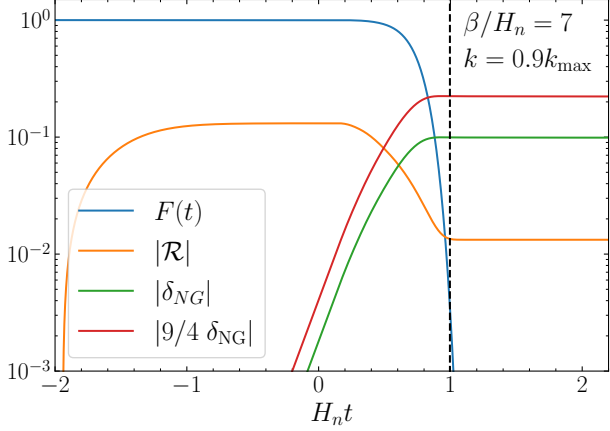


FIG. 1. Time evolution of the absolute value of the false vacuum fraction $F(t)$, the comoving curvature perturbation \mathcal{R} , and the density contrast δ_{NG} of an independently evolving volume $4\pi k^{-3}/3$, where $k = 0.9k_{\text{max}}$ and $\beta/H_n = 7$. The value of $9/4 \delta_{\text{NG}}$ is given for reference. The dashed line represents the time when the $k = 0.9k_{\text{max}}$ mode re-enters the horizon.

δP_{rel} , we utilize Eq. (17) and Eq. (18) to perform the calculation.

It should be noted that S_{Vr} becomes divergent when $\dot{\rho}_r = 0$, as indicated by Eq. (18). This is because ρ_r initially increases immediately after the onset of the FOPT and subsequently decreases around the percolation time due to cosmic expansion. However, when S_{Vr} is combined with the $\dot{\rho}V\dot{\rho}_r$ term in Eq. (17), the divergence is canceled, resulting in a well-behaved integration. After obtaining ζ for different Hubble patches, the comoving curvature perturbations can be computed using the approximation at super-horizon scales $\mathcal{R} \approx -\zeta$.

B. Results

We show the time evolution of the averaged comoving curvature perturbation \mathcal{R} and density contrast δ in an independently evolving box of size $4\pi k^{-3}/3$ in Fig. 1, where $k = 0.9k_{\text{max}}$. It is clear that there is no definite relation between δ_{NG} and \mathcal{R} , and that the approximate relation for super-horizon perturbations of the radiation fluid $\mathcal{R} \approx -(9/4)\delta_C$ [36] for comoving density contrast δ_C breaks down, suggesting that δ can not be approximately identified as the value in the comoving gauge.

We also present in Fig. 2 the variance of the resulting comoving curvature perturbations for various values of k/k_{max} and β/H_n . The magnitude of the variance is consistent with that reported in Ref. [20] and is significantly smaller than that found in [24]. The variance also exhibits the expected asymptotic behavior (see [19] for details), scaling as k^3 at small k and as β^{-5} at large β . However, for large β , small deviations from the k^3 scaling are observed, as shown in the right panel of Fig. 2. These

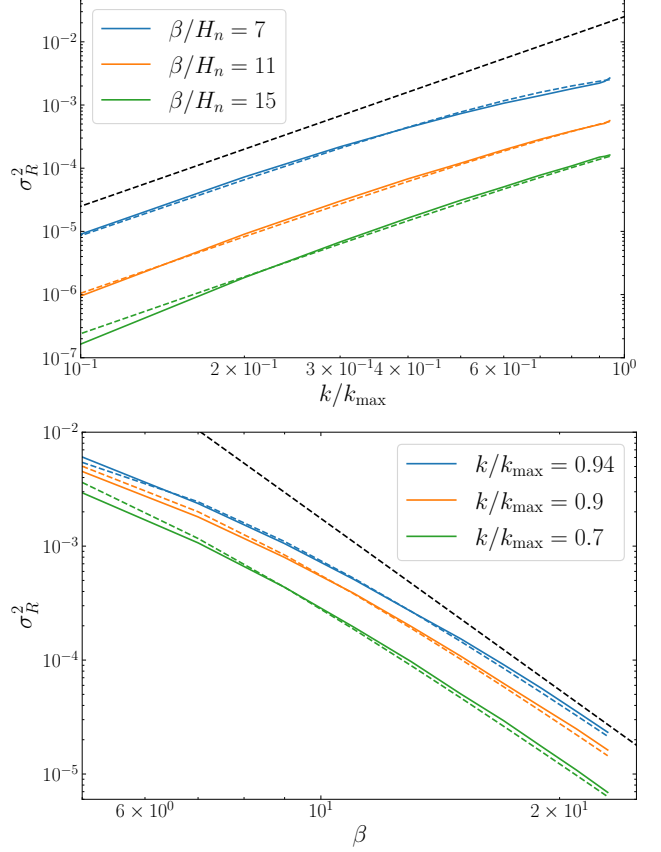


FIG. 2. Variance of the comoving curvature perturbations $\sigma_{\mathcal{R}}^2$ as a function of β and k/k_{max} . The dashed curves represent the corresponding fits, while the dashed black lines indicate the β^{-5} and k^3 reference power laws.

deviations are likely attributable to the limited number of bubbles employed in the simulations.

Additionally, employing the approximated relation $\mathcal{R} \approx -(9/4)\delta_C$ on super-horizon scales, we estimate the probability distribution of the comoving density contrast, δ_C , a key quantity for quantifying the PBH abundance. The results for $k = 0.9k_{\text{max}}$ are presented in Fig. 3. PBHs are believed to form from the positive tail of the δ_C distribution exceeding a critical threshold, δ_{crit} . The precise value of δ_{crit} remains a subject of active investigation, since they may have a complicated dependence on the shape of the perturbation [44–46]; here, we adopt a typical value of $\delta_{\text{crit}} \approx 0.45$, as depicted in Fig. 3. A comparison of the δ_C distribution with this formation threshold indicates that PBHs are unlikely to be produced from the curvature perturbations generated by these FOPTs.

To accommodate the broader interests of phenomenological studies, we provide a fitting formula for $P_{\mathcal{R}}$. We first fit $\sigma_{\mathcal{R}}^2$ (see the fitting results in Fig. 2), ensuring that the employed formula exhibits the correct asymptotic behavior. Using the approximate relation

$$\sigma_{\mathcal{R}}^2 = \int d\ln k W^2(kR) P_{\mathcal{R}}(k) \simeq \frac{3\pi}{2} P_{\mathcal{R}}(k = R^{-1}), \quad (19)$$

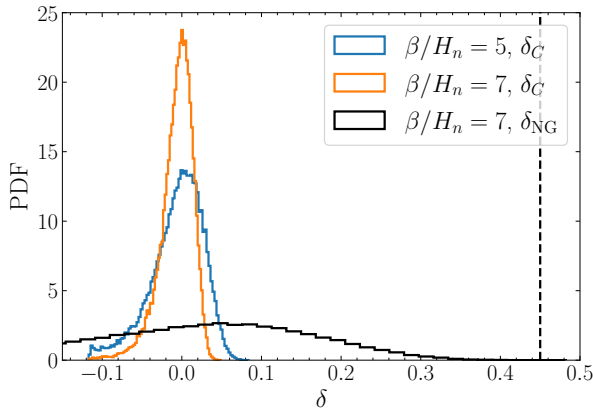


FIG. 3. Distributions of density contrast of independently evolving volumes $4\pi k^{-3}/3$, where $k = 0.9k_{\max}$. The blue and orange envelopes represent δ_C , the density contrast in the comoving-gauge. The black envelope represents the density contrast computed from separate universe simulations (δ_{NG}). The PBH formation threshold $\delta_{\text{crit}} \approx 0.45$ is marked as a vertical dashed line.

which holds for the top-hat window function $W(x) = 3(\sin x - x \cos x)/x^3$ and assumes $P_{\mathcal{R}} \propto k^3$ on super-horizon scales, we derive the fitting formula for $P_{\mathcal{R}}$ as

$$P_{\mathcal{R}}(k) = A \left(\frac{\alpha}{1 + \alpha} \right)^2 \frac{(k/k_{\max})^3 (\beta/H_n)^{-3}}{[a + (k/k_{\max})^2 (\beta/H_n)^{-2}]^3} \times \frac{1}{(b + \beta/H_n)^2} \Theta(k_{\max} - k), \quad (20)$$

where Θ is the heaviside step function and $\alpha \approx \Delta V/\rho_r$ represents the phase transition strength, and the parameters are set to $A = 0.0038$, $a = 0.043$, and $b = 1.77$. The peak wave number k_{\max} and the reheating temperature T_{reh} are related by

$$\begin{aligned} k_{\max} &= \frac{\pi T_0}{3\sqrt{10} M_{\text{pl}}} \frac{T_{\text{reh}}}{\left(\frac{g_s(T_{\text{reh}})}{g_s(T_0)} \right)^{1/3}} g_{\rho}^{1/2}(T_{\text{reh}}) \\ &= 1.61 \times 10^7 \text{ Mpc}^{-1} \left(\frac{g_s(T_{\text{reh}})}{68.74} \right)^{-1/3} \times \left(\frac{g_{\rho}(T_{\text{reh}})}{69.76} \right)^{1/2} \left(\frac{T_{\text{reh}}}{\text{GeV}} \right). \end{aligned} \quad (21)$$

In the above equation, $T_0 = 2.35 \times 10^{-13}$ GeV is the temperature of CMB, and g_{ρ} and g_s denote the effective degrees of freedom for the energy density and entropy density, where we adopt the values from Ref. [47].

V. OBSERVATIONAL CONSEQUENCES

While inhomogeneities arising from FOPTs may be insufficient to generate PBHs, direct or indirect limits on primordial curvature perturbations from various astrophysical and cosmological probes, can be employed to

constrain FOPTs. Furthermore, when the corresponding modes re-enter the horizon following thermal inflation, SIGWs can arise as a direct consequence of curvature perturbations. In this section, we briefly discuss potential constraints on $P_{\mathcal{R}}(k)$ and the implications for FOPT parameters in the presence of SIGWs based on PTA data.

A. Observational constraints on $P_{\mathcal{R}}$

The primordial curvature power spectrum, $P_{\mathcal{R}}(k)$, produced by FOPTs is subject to various constraints. On large scales with modes $k \lesssim 3 \text{ Mpc}^{-1}$, CMB anisotropy observations [37] and Lyman- α measurements [38] restrict the spectrum to $P_{\mathcal{R}} \simeq \mathcal{O}(10^{-9})$. Enhancements of $P_{\mathcal{R}}$ on small scales can generate observable signals via CMB spectral distortions and SIGWs. The Far Infrared Absolute Spectrophotometer (FIRAS) has constrained the primordial power spectrum in the range of $10 \text{ Mpc}^{-1} \lesssim k \lesssim 10^5 \text{ Mpc}^{-1}$ through spectral observations of the CMB [39]. Pulsar timing arrays and the upcoming Square Kilometer Array (SKA) telescope provide current limits and projected constraints for larger modes in the range $10^5 \text{ Mpc}^{-1} \lesssim k \lesssim 10^{10} \text{ Mpc}^{-1}$ [40]. The next generation of gravitational wave observatories such as LISA will extend the sensitivity to even larger modes, covering the range $10^{10} \text{ Mpc}^{-1} \lesssim k \lesssim 10^{15} \text{ Mpc}^{-1}$ [41]. The formation of small dark matter structures, known as ultra-compact mini-halos (UCMHs), serves as an indirect probe of the primordial power spectrum. Assuming dark matter consists of weakly interacting massive particles (WIMPs) that annihilate into Standard Model particles, the presence of UCMHs can be effectively traced through γ -ray and neutrino observations [42, 48–50], as well as imprints on CMB anisotropies resulting from extra energy injection [43].

In Fig. 4, we present these existing and forecasted constraints together with benchmark $P_{\mathcal{R}}(k)$ s for varying β/H_n and T_{reh} . In table I, we further translate various constraints into $T_{\text{reh}} - \beta/H_n$ plane using a monochromatic power spectrum $P_{\mathcal{R}}(k = k_{\max})$. However, since these constraints are obtained from a spiky power-spectrum enhancement, their applicability to $P_{\mathcal{R}}(k)$ from FOPTs requires further investigation. Moreover, the constraints from UCMHs [42, 43] are based on the assumption that WIMP dark matter annihilates into $b\bar{b}$ with a mass $m_{\text{DM}} = 1 \text{ TeV}$ and s -wave thermal relic cross section $\langle \sigma v \rangle_0 = 3 \times 10^{-26} \text{ cm}^3 \text{s}^{-1}$. Otherwise, the corresponding limits would be significantly relaxed.

B. Scalar-induced gravitational waves

The SIGWs produced by these curvature perturbations can represent a significant secondary source of phase transition gravitational waves [24], distinct from the primary gravitational waves produced by the dynamics of

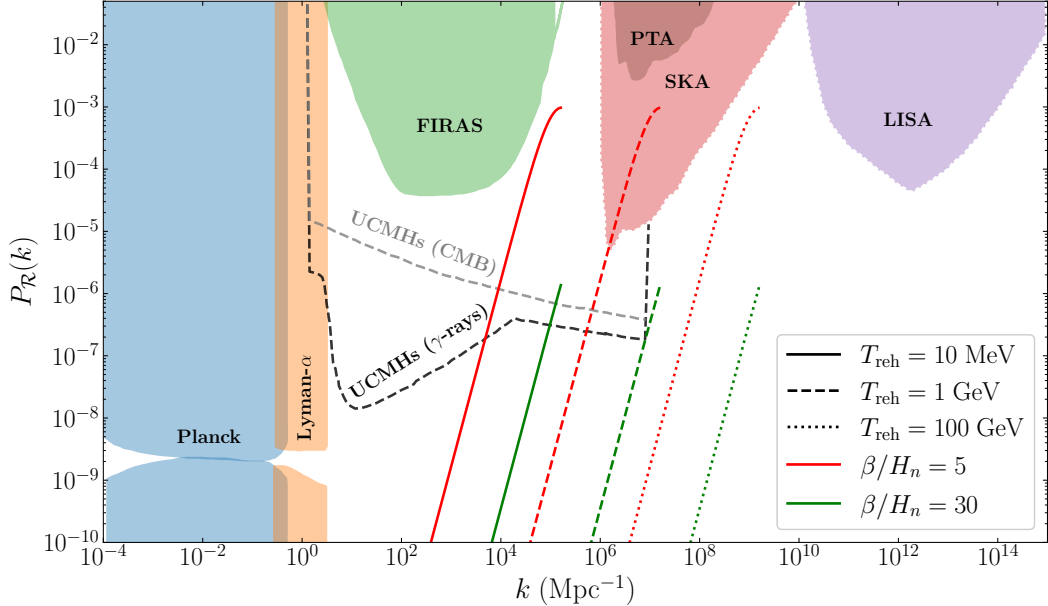


FIG. 4. Various benchmark spectra $P_R(k)$ for $\alpha = 10$ with varying β/H_n and T_{reh} . Also displayed is a compilation of existing constraints on the primordial power spectrum $P_R(k)$ (solid-outlined filled regions), sensitivity forecasts for next-generation observatories (dotted-outlined filled regions), and UCMH-based constraints (dashed lines). The non-UCMH constraints are derived from CMB anisotropies [37] (light blue), Lyman- α observations [38] (orange), CMB spectral distortions [39] (green), Pulsar Timing Arrays [40] (red), as well as SKA and LISA forecasts [41] (pink and purple). The UCMH-based constraints, which assume a monochromatic power-spectrum enhancement and that WIMP dark matter annihilates into $b\bar{b}$ with a mass $m_{\text{DM}} = 1 \text{ TeV}$ and s -wave thermal relic cross section $\langle\sigma v\rangle_0 = 3 \times 10^{-26} \text{ cm}^3 \text{ s}^{-1}$, are obtained from diffuse γ -ray searches [42] (black dashed line) and limits on extra energy injection into the CMB [43] (gray dashed line).

| | UCMHs (γ -ray) | UCMHs (CMB) | FIRAS | SKA | LISA |
|-----------------------------|-----------------------------|-----------------------------|--|------------------------------|--------------------------------------|
| $T_{\text{reh}}/\text{GeV}$ | $(3.4 \times 10^{-7}, 0.6)$ | $(3.4 \times 10^{-7}, 0.6)$ | $(1.2 \times 10^{-6}, 5.1 \times 10^{-3})$ | $(8.3 \times 10^{-2}, 35.6)$ | $(1.7 \times 10^3, 8.4 \times 10^6)$ |
| β/H_n | $\gtrsim 35 - 80$ | $\gtrsim 20 - 40$ | $\gtrsim 3 - 15$ | $\gtrsim 3 - 23$ | $\gtrsim 4 - 14$ |

TABLE I. Similar to Fig. 4, but translates various constraints into $T_{\text{reh}} - \beta/H_n$ plane using a monochromatic power spectrum $P_R(k = k_{\text{max}})$.

phase transitions, such as bubble collisions [51], sound waves [6], or turbulence [52], et. al.

The spectrum of the SIGW can be computed from

$$\begin{aligned} \Omega_{\text{SIGW}} h^2 &= \Omega_{r,0} h^2 \frac{g_\rho(T_{\text{reh}})}{g_\rho(T_0)} \left(\frac{g_s(T_{\text{reh}})}{g_s(T_0)} \right)^{-4/3} \Omega_{\text{SIGW}}(T_{\text{reh}}) \\ &= 1.65 \times 10^{-5} \left(\frac{\Omega_{r,0} h^2}{4.18 \times 10^{-5}} \right) \left(\frac{g_\rho(T_{\text{reh}})}{100} \right) \\ &\quad \times \left(\frac{g_s(T_{\text{reh}})}{100} \right)^{-4/3} \Omega_{\text{SIGW}}(T_{\text{reh}}), \end{aligned} \quad (22)$$

where $\Omega_{r,0} h^2$ is the energy density ratio of radiation today. The quantity $\Omega_{\text{SIGW}}(T_{\text{reh}})$ characterizes the induced gravitational waves at the reheating temperature T_{reh} [53, 54],

$$\Omega_{\text{SIGW}}(T_{\text{reh}}) = \int_0^\infty dv \int_{|1-v|}^{1+v} du T_{\text{RD}}(u, v) P_R(ku) P_R(kv), \quad (23)$$

and the transfer function T_{RD} is defined as

$$\begin{aligned} T_{\text{RD}}(u, v) &= \left(\frac{4v^2 - (1 - u^2 + v^2)^2}{4u^2 v^2} \right)^2 y^2 \\ &\quad \times \left\{ \frac{\pi^2}{4} y^2 \Theta[u + v - c_r^{-1}] + \left(1 - \frac{1}{2} y \ln \left| \frac{1+y}{1-y} \right| \right)^2 \right\}, \end{aligned} \quad (24)$$

with $y = (u^2 + v^2 - c_r^{-2})/(2uv)$.

The total observed GW spectrum is then composed of a primary component and a secondary component from SIGWs:

$$\Omega_{\text{total}} h^2 = \Omega_{\text{primary}} h^2 + \Omega_{\text{SIGW}} h^2. \quad (25)$$

As an example, we investigate two typical FOPT models: bubble collisions (PT-BUBBLE) and sound waves (PT-SOUND). The fitting formulas for the GWs in both models, detailed in [18], share the same broken power-law

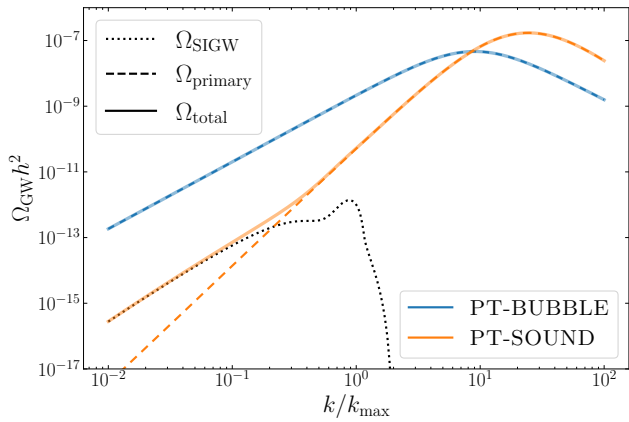


FIG. 5. GWs spectra from PT-BUBBLE and PT-SOUND models as the primary GW sources together with SIGWs from curvature perturbations.

shape function:

$$S(x) = \frac{(a+b)^c}{(bx^{-a/c} + ax^{b/c})^c}, \quad (26)$$

where a , b , and c are shape parameters. In Fig. 5, we present both the primary and secondary GW spectra, calculated with phase transition parameters $\alpha = 10$, $\beta/H_n = 7$, and $T_{\text{reh}} = 0.05$ GeV. The shape parameters are set to their best-fit values from the NANOGrav 15-year dataset [18]: $a = 2.04$, $b = 1.97$, $c = 2.03$ for PT-BUBBLE, and $a = 3.58$, $b = 2.87$, $c = 4.16$ for PT-SOUND. Fig. 5 clearly illustrates that the SIGW spectrum peaks at a larger scale compared to the primary one. However, our gauge-invariant calculation suggests that this potential secondary SGWB source is likely sub-dominant compared to the primary source. Including this secondary component may only introduce marginal modifications at low frequencies for the PT-SOUND model.

To further investigate the impact of SIGWs on parameter estimation, we analyze NANOGrav 15-year data and illustrate the modifications introduced by this secondary source. Our analysis focuses on three phase transition parameters: the strength α , the reheating temperature T_{reh} , and the nucleation rate β/H_n . We employ the PTArcade code [55, 56] to derive posterior distributions for these model parameters. The results for the PT-BUBBLE and PT-SOUND models are presented in Fig. 6. We observe negligible modifications to the posterior distributions for the PT-BUBBLE model and only marginal changes for the PT-SOUND model. The small alterations of the PT-SOUND result from the low-frequency modifications introduced by the SIGW. Overall, we conclude that the inclusion of GWs induced by super-horizon curvature perturbations does not significantly affect the interpretation of the FOPT models in the context of current PTA data.

VI. CONCLUSIONS

Slow and strongly supercooled FOPTs, which are favored by recent PTA data, can generate super-horizon inhomogeneities. In this study, we performed a gauge-invariant calculation of the curvature perturbations induced by these inhomogeneities. Our results indicate that the inhomogeneities derived from separate universe simulations cannot be interpreted as perturbations within the comoving gauge, a choice commonly employed to assess the abundance PBHs. Furthermore, the distribution of the density contrast, estimated from the gauge-invariant comoving curvature perturbations, exhibits a positive tail that remains significantly below the conventional PBH formation threshold. Consequently, we conclude that the formation of PBHs through this mechanism is highly unlikely.

We also present an empirical template for these super-horizon curvature perturbations, which can be utilized to compute potential cosmological observables. As a demonstration, we examine the consistency of $P_{\mathcal{R}}$ generated by FOPTs with current and future constraints on primordial curvature perturbations. Our results indicate that slow FOPTs may be constrained by future SKA data, whereas relatively fast FOPTs are subject to constraints derived from UCMH observations. We also calculate the SIGWs generated by these perturbations, representing a potential secondary GW source. However, owing to the suppressed amplitude of the curvature perturbations, this secondary GW source has only a marginal impact on phase transition models constrained by the NANOGrav 15-year data.

In summary, this study proposes a new framework for quantifying the large-scale gravitational effects of FOPTs as curvature perturbations. Our gauge-invariant analysis disfavors both the formation of PBHs and a significant secondary GW source by SIGW via this mechanism. The template for the comoving curvature perturbations presented in this work can be applied to future investigations of other potential observables originating from the large-scale inhomogeneities associated with FOPTs.

ACKNOWLEDGMENTS

The authors thank Ryusuke Jinno, Shaojiang Wang and Ke-pan Xie for fruitful discussions. X.W. and C.B. are supported by Australian Research Council grants DP220100643 and LE250100010. R.D. is supported in part by the National Key R&D Program of China (No. 2021YFC2203100). C.T. is supported by the National Natural Science Foundation of China (Grants No. 12405048) and the Natural Science Foundation of Anhui Province (Grants No. 2308085QA34).

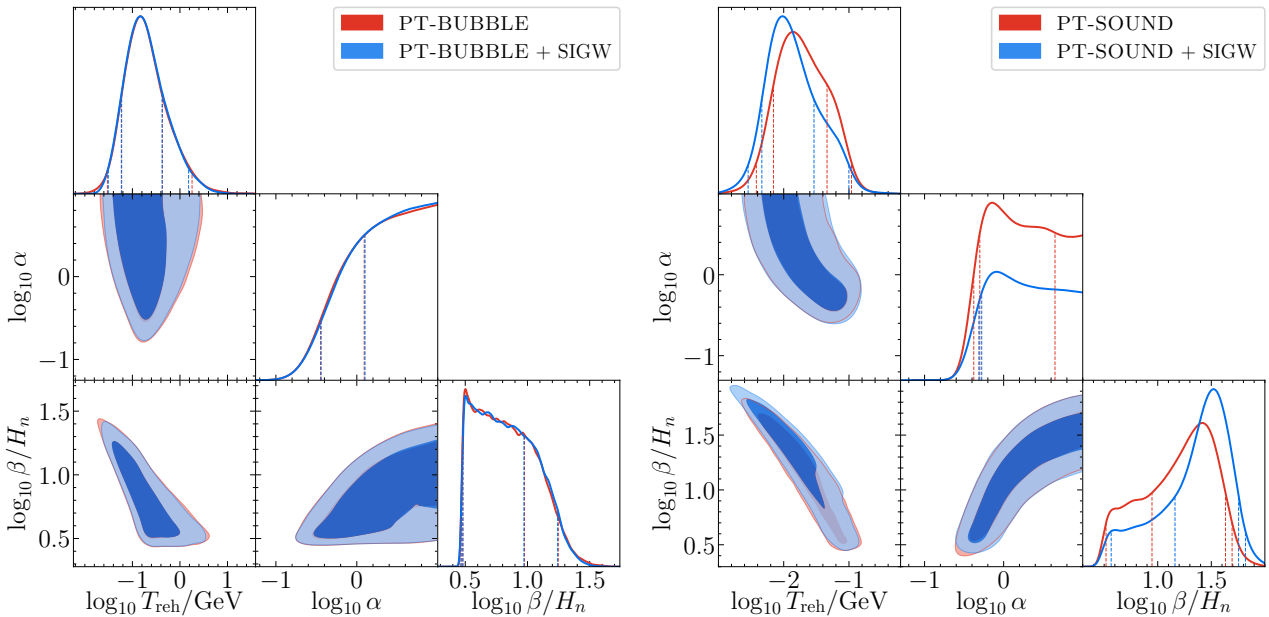


FIG. 6. Posterior distributions of phase transition parameters from NANOGrav-15 data, based on PT-BUBBLE (left) and PT-SOUND (right) models, with and without considering SIGW introduced by curvature perturbations. The contours show both the 68% (darker) and 95% (lighter) Bayesian credible regions. And the vertical lines in the 1D marginalized distributions also represent 68% and 95% Bayesian credible intervals.

[1] V. A. Kuzmin, V. A. Rubakov, and M. E. Shaposhnikov, On the Anomalous Electroweak Baryon Number Non-conservation in the Early Universe, *Phys. Lett. B* **155**, 36 (1985).

[2] A. G. Cohen, D. B. Kaplan, and A. E. Nelson, Progress in electroweak baryogenesis, *Ann. Rev. Nucl. Part. Sci.* **43**, 27 (1993), [arXiv:hep-ph/9302210](https://arxiv.org/abs/hep-ph/9302210).

[3] V. A. Rubakov and M. E. Shaposhnikov, Electroweak baryon number nonconservation in the early universe and in high-energy collisions, *Usp. Fiz. Nauk* **166**, 493 (1996), [arXiv:hep-ph/9603208](https://arxiv.org/abs/hep-ph/9603208).

[4] A. Riotto and M. Trodden, Recent progress in baryogenesis, *Ann. Rev. Nucl. Part. Sci.* **49**, 35 (1999), [arXiv:hep-ph/9901362](https://arxiv.org/abs/hep-ph/9901362).

[5] D. E. Morrissey and M. J. Ramsey-Musolf, Electroweak baryogenesis, *New J. Phys.* **14**, 125003 (2012), [arXiv:1206.2942 \[hep-ph\]](https://arxiv.org/abs/1206.2942).

[6] M. Hindmarsh, S. J. Huber, K. Rummukainen, and D. J. Weir, Gravitational waves from the sound of a first order phase transition, *Phys. Rev. Lett.* **112**, 041301 (2014), [arXiv:1304.2433 \[hep-ph\]](https://arxiv.org/abs/1304.2433).

[7] C. Caprini *et al.*, Detecting gravitational waves from cosmological phase transitions with LISA: an update, *JCAP* **03**, 024, [arXiv:1910.13125 \[astro-ph.CO\]](https://arxiv.org/abs/1910.13125).

[8] P. Athron, C. Balázs, A. Fowlie, L. Morris, and L. Wu, Cosmological phase transitions: From perturbative particle physics to gravitational waves, *Prog. Part. Nucl. Phys.* **135**, 104094 (2024), [arXiv:2305.02357 \[hep-ph\]](https://arxiv.org/abs/2305.02357).

[9] C. Tian, X. Wang, and C. Balázs, Gravitational waves from cosmological first-order phase transitions with precise hydrodynamics, *Eur. Phys. J. C* **85**, 1091 (2025), [arXiv:2409.14505 \[hep-ph\]](https://arxiv.org/abs/2409.14505).

[10] X. Wang, C. Tian, and C. Balázs, Self-consistent prediction of gravitational waves from cosmological phase transitions, (2024), [arXiv:2409.06599 \[hep-ph\]](https://arxiv.org/abs/2409.06599).

[11] C. Tian, X. Wang, and C. Balázs, DeepSSM: an emulator of gravitational wave spectra from sound waves during cosmological first-order phase transitions, *JCAP* **08**, 060, [arXiv:2501.10244 \[astro-ph.CO\]](https://arxiv.org/abs/2501.10244).

[12] C. Balázs, X. Wang, and C. Tian, Gravitational waves from cosmological first-order phase transitions with self-consistent hydrodynamics, *PoS CORFU2024*, 261 (2025).

[13] G. Agazie *et al.* (NANOGrav), The NANOGrav 15 yr Data Set: Evidence for a Gravitational-wave Background, *Astrophys. J. Lett.* **951**, L8 (2023), [arXiv:2306.16213 \[astro-ph.HE\]](https://arxiv.org/abs/2306.16213).

[14] H. Xu *et al.*, Searching for the Nano-Hertz Stochastic Gravitational Wave Background with the Chinese Pulsar Timing Array Data Release I, *Res. Astron. Astrophys.* **23**, 075024 (2023), [arXiv:2306.16216 \[astro-ph.HE\]](https://arxiv.org/abs/2306.16216).

[15] J. Antoniadis *et al.* (EPTA, InPTA:), The second data release from the European Pulsar Timing Array - III. Search for gravitational wave signals, *Astron. Astrophys.* **678**, A50 (2023), [arXiv:2306.16214 \[astro-ph.HE\]](https://arxiv.org/abs/2306.16214).

[16] D. J. Reardon *et al.*, Search for an Isotropic Gravitational-wave Background with the Parkes Pulsar Timing Array, *Astrophys. J. Lett.* **951**, L6 (2023), [arXiv:2306.16215 \[astro-ph.HE\]](https://arxiv.org/abs/2306.16215).

[17] M. T. Miles *et al.*, The MeerKAT Pulsar Timing Array: the first search for gravitational waves with the MeerKAT radio telescope, *Mon. Not. Roy. Astron. Soc.* **536**, 1489

(2024), arXiv:2412.01153 [astro-ph.HE].

[18] A. Afzal *et al.* (NANOGrav), The NANOGrav 15 yr Data Set: Search for Signals from New Physics, *Astrophys. J. Lett.* **951**, L11 (2023), [Erratum: *Astrophys.J.Lett.* 971, L27 (2024), Erratum: *Astrophys.J.* 971, L27 (2024)], arXiv:2306.16219 [astro-ph.HE].

[19] J. Liu, L. Bian, R.-G. Cai, Z.-K. Guo, and S.-J. Wang, Constraining First-Order Phase Transitions with Curvature Perturbations, *Phys. Rev. Lett.* **130**, 051001 (2023), arXiv:2208.14086 [astro-ph.CO].

[20] G. Franciolini, Y. Gouttenoire, and R. Jinno, Curvature Perturbations from First-Order Phase Transitions: Implications to Black Holes and Gravitational Waves, (2025), arXiv:2503.01962 [hep-ph].

[21] R.-G. Cai, Y.-S. Hao, and S.-J. Wang, Primordial black holes and curvature perturbations from false vacuum islands, *Sci. China Phys. Mech. Astron.* **67**, 290411 (2024), arXiv:2404.06506 [astro-ph.CO].

[22] C. Fu and J. Liu, The power of SKA to Constrain cosmological gravitational-wave backgrounds below the astrophysical foreground noise, (2025), arXiv:2506.14366 [astro-ph.CO].

[23] Y. Gouttenoire, WIMPs and new physics interpretations of the PTA signal are incompatible, (2025), arXiv:2503.03857 [hep-ph].

[24] M. Lewicki, P. Toczek, and V. Vaskonen, Black Holes and Gravitational Waves from Slow First-Order Phase Transitions, *Phys. Rev. Lett.* **133**, 221003 (2024), arXiv:2402.04158 [astro-ph.CO].

[25] J. Liu, L. Bian, R.-G. Cai, Z.-K. Guo, and S.-J. Wang, Primordial black hole production during first-order phase transitions, *Phys. Rev. D* **105**, L021303 (2022), arXiv:2106.05637 [astro-ph.CO].

[26] K. Kawana, T. Kim, and P. Lu, PBH formation from overdensities in delayed vacuum transitions, *Phys. Rev. D* **108**, 103531 (2023), arXiv:2212.14037 [astro-ph.CO].

[27] Y. Gouttenoire and T. Volansky, Primordial black holes from supercooled phase transitions, *Phys. Rev. D* **110**, 043514 (2024), arXiv:2305.04942 [hep-ph].

[28] M. S. Turner, E. J. Weinberg, and L. M. Widrow, Bubble nucleation in first order inflation and other cosmological phase transitions, *Phys. Rev. D* **46**, 2384 (1992).

[29] X. Wang, F. P. Huang, and X. Zhang, Phase transition dynamics and gravitational wave spectra of strong first-order phase transition in supercooled universe, *JCAP* **05**, 045, arXiv:2003.08892 [hep-ph].

[30] G. Elor, R. Jinno, S. Kumar, R. McGehee, and Y. Tsai, Finite Bubble Statistics Constrain Late Cosmological Phase Transitions, *Phys. Rev. Lett.* **133**, 211003 (2024), arXiv:2311.16222 [hep-ph].

[31] D. Wands, K. A. Malik, D. H. Lyth, and A. R. Liddle, A New approach to the evolution of cosmological perturbations on large scales, *Phys. Rev. D* **62**, 043527 (2000), arXiv:astro-ph/0003278.

[32] K. A. Malik, D. Wands, and C. Ungarelli, Large scale curvature and entropy perturbations for multiple interacting fluids, *Phys. Rev. D* **67**, 063516 (2003), arXiv:astro-ph/0211602.

[33] K. A. Malik and D. Wands, Adiabatic and entropy perturbations with interacting fluids and fields, *JCAP* **02**, 007, arXiv:astro-ph/0411703.

[34] J. M. Bardeen, Gauge Invariant Cosmological Perturbations, *Phys. Rev. D* **22**, 1882 (1980).

[35] V. F. Mukhanov, H. A. Feldman, and R. H. Brandenberger, Theory of cosmological perturbations. Part 1. Classical perturbations. Part 2. Quantum theory of perturbations. Part 3. Extensions, *Phys. Rept.* **215**, 203 (1992).

[36] A. M. Green, A. R. Liddle, K. A. Malik, and M. Sasaki, A New calculation of the mass fraction of primordial black holes, *Phys. Rev. D* **70**, 041502 (2004), arXiv:astro-ph/0403181.

[37] N. Aghanim *et al.* (Planck), Planck 2018 results. VI. Cosmological parameters, *Astron. Astrophys.* **641**, A6 (2020), [Erratum: *Astron.Astrophys.* 652, C4 (2021)], arXiv:1807.06209 [astro-ph.CO].

[38] S. Bird, H. V. Peiris, M. Viel, and L. Verde, Minimally Parametric Power Spectrum Reconstruction from the Lyman-alpha Forest, *Mon. Not. Roy. Astron. Soc.* **413**, 1717 (2011), arXiv:1010.1519 [astro-ph.CO].

[39] J. Chluba, A. L. Erickcek, and I. Ben-Dayan, Probing the inflaton: Small-scale power spectrum constraints from measurements of the CMB energy spectrum, *Astrophys. J.* **758**, 76 (2012), arXiv:1203.2681 [astro-ph.CO].

[40] C. T. Byrnes, P. S. Cole, and S. P. Patil, Steepest growth of the power spectrum and primordial black holes, *JCAP* **06**, 028, arXiv:1811.11158 [astro-ph.CO].

[41] K. Inomata and T. Nakama, Gravitational waves induced by scalar perturbations as probes of the small-scale primordial spectrum, *Phys. Rev. D* **99**, 043511 (2019), arXiv:1812.00674 [astro-ph.CO].

[42] M. S. Delos, A. L. Erickcek, A. P. Bailey, and M. A. Alvarez, Density profiles of ultracompact minihalos: Implications for constraining the primordial power spectrum, *Phys. Rev. D* **98**, 063527 (2018), arXiv:1806.07389 [astro-ph.CO].

[43] G. Franco Abellán and G. Facchinetti, Minihalos as probes of the inflationary spectrum: accurate boost factor calculation and new CMB constraints, *JCAP* **06**, 032, arXiv:2304.02996 [astro-ph.CO].

[44] A. Escrivà, PBH Formation from Spherically Symmetric Hydrodynamical Perturbations: A Review, *Universe* **8**, 66 (2022), arXiv:2111.12693 [gr-qc].

[45] I. Musco, Threshold for primordial black holes: Dependence on the shape of the cosmological perturbations, *Phys. Rev. D* **100**, 123524 (2019), arXiv:1809.02127 [gr-qc].

[46] A. Escrivà, C. Germani, and R. K. Sheth, Universal threshold for primordial black hole formation, *Phys. Rev. D* **101**, 044022 (2020), arXiv:1907.13311 [gr-qc].

[47] K. Saikawa and S. Shirai, Precise WIMP Dark Matter Abundance and Standard Model Thermodynamics, *JCAP* **08**, 011, arXiv:2005.03544 [hep-ph].

[48] A. S. Josan and A. M. Green, Gamma-rays from ultracompact minihalos: potential constraints on the primordial curvature perturbation, *Phys. Rev. D* **82**, 083527 (2010), arXiv:1006.4970 [astro-ph.CO].

[49] T. Bringmann, P. Scott, and Y. Akrami, Improved constraints on the primordial power spectrum at small scales from ultracompact minihalos, *Phys. Rev. D* **85**, 125027 (2012), arXiv:1110.2484 [astro-ph.CO].

[50] T. Nakama, T. Suyama, K. Kohri, and N. Hiroshima, Constraints on small-scale primordial power by annihilation signals from extragalactic dark matter minihalos, *Phys. Rev. D* **97**, 023539 (2018), arXiv:1712.08820 [astro-ph.CO].

[51] S. J. Huber and T. Konstandin, Gravitational Wave Production by Collisions: More Bubbles, *JCAP* **09**, 022,

arXiv:0806.1828 [hep-ph].

[52] C. Caprini, R. Durrer, and G. Servant, The stochastic gravitational wave background from turbulence and magnetic fields generated by a first-order phase transition, *JCAP* **12**, 024, arXiv:0909.0622 [astro-ph.CO].

[53] K. Kohri and T. Terada, Semianalytic calculation of gravitational wave spectrum nonlinearly induced from primordial curvature perturbations, *Phys. Rev. D* **97**, 123532 (2018), arXiv:1804.08577 [gr-qc].

[54] J. R. Espinosa, D. Racco, and A. Riotto, A Cosmological Signature of the SM Higgs Instability: Gravitational Waves, *JCAP* **09**, 012, arXiv:1804.07732 [hep-ph].

[55] A. Mitridate, D. Wright, R. von Eckardstein, T. Schröder, J. Nay, K. Olum, K. Schmitz, and T. Trickle, PTArcade, (2023), arXiv:2306.16377 [hep-ph].

[56] A. Mitridate, Ptarcade 10.5281/zenodo.7876430 (2023).